JOURNAL OF THE ROYAL SOCIETY Interface

rsif.royalsocietypublishing.org

Research

Cite this article: Subbiah R, Ramasundaram S, Du P, Hyojin K, Sung D, Park K, Lee N-E, Yun K, Choi KJ. 2013 Evaluation of cytotoxicity, biophysics and biomechanics of cells treated with functionalized hybrid nanomaterials. J R Soc Interface 10: 20130694.
http://dx.doi.org/10.1098/rsif.2013.0694

Received: 29 July 2013
Accepted: 8 August 2013

Subject Areas:
nanotechnology, biomedical engineering, biomechanics

Keywords:
functionalization, atomic force microscopy–force spectroscopy, cellular interaction, cytotoxicity, biophysics, biomechanics

Authors for correspondence:
Kyusik Yun
e-mail: ykyusik@gachon.ac.kr
Kyoung Jin Choi
e-mail: choi@unist.ac.kr

Electronic supplementary material is available at http://dx.doi.org/10.1098/rsif.2013.0694 or via http://rsif.royalsocietypublishing.org.

Royal Society Publishing
Informing the science of the future

Evaluation of cytotoxicity, biophysics and biomechanics of cells treated with functionalized hybrid nanomaterials

Ramesh Subbiah[1,2], Subramaniyan Ramasundaram[3], Ping Du[1,2], Kim Hyojin[2], Dongkyung Sung[4], Kwideok Park[1,2], Nae-Eung Lee[3], Kyusik Yun[5] and Kyoung Jin Choi[6]

[1]Department of Biomedical Engineering, University of Science and Technology (UST), 113 Gwahangno, Daejon, South Korea
[2]Center for Biomaterials, Korea Institute of Science and Technology (KIST) Seoul, Seoul, South Korea
[3]School of Advanced Materials Science and Engineering, Sungkyunkwan University, Suwon, South Korea
[4]Department of Biomedical Engineering, Samsung Hospital, Seoul, South Korea
[5]Department of Bionano Technology, Gachon University, Seongnam, South Korea
[6]School of Mechanical and Advanced Materials Engineering, Ulsan National Institute of Science and Technology (UNIST), Ulsan, South Korea

Hybrids consisting of carboxylated, single-walled carbon nanotube (c-SWNT)–silver nanoparticles (AgNPs)-DNA–poly vinyl alcohol (PVA) are synthesized via sequential functionalization to mimic the theragnostic (therapy and diagnosis) system. Carboxylation of SWNT has minimized the metal impurities with plenty of –COOH groups to produce hybrid (c-SWNT-AgNPs). The hybrid is further wrapped with DNA (hybrid-DNA) and encapsulated with PVA as hybrid composite (HC). Materials were tested against human alveolar epithelial cells (A549), mouse fibroblasts cells (NIH3T3) and human bone marrow stromal cells (HS-5). The composition-sensitive physico-chemical interactions, biophysics and biomechanics of materials-treated cells are evaluated. The cell viability was improved for HC, hybrid-PVA and c-SWNT when compared with SWNT and hybrid. SWNT and hybrid showed cell viability less than 60% at high dose (40 $\mu g\ ml^{-1}$) and hybrid-PVA and HC retained 80% or more cell viability. The treatment of hybrid nanomaterials considerably changed cell morphology and intercellular interaction with respect to the composition of materials. Peculiarly, PVA-coated hybrid was found to minimize the growth of invadopodia of A549 cells, which is responsible for the proliferation of cancer cells. Surface roughness of cells increased after treatment with hybrid, where cytoplasmic regions specifically showed higher roughness. Nanoindentation results suggest that changes in biomechanics occurred owing to possible internalization of the hybrid. The changes in force spectra of treated cells indicated a possible greater interaction between the cells and hybrid with distinct stiffness and demonstrated the surface adherence and internalization of hybrid on or inside the cells.

1. Introduction

The unique nanoscale structure, physiochemical properties, ultrahigh mechanical strength, high electrical and thermal conductivity and the ability to store therapeutics in the vesicle-like structure of carbon nanotubes (CNTs) have been a source of interest for scientific and industrial research [1,2]. Proper tuning and sensing the distinctive properties of CNTs alleviate the synthesis of various hybrids with multifunctionality. Their carbonaceous nature, resonance Raman scattering, photoluminescence, strong near-infrared optical absorption, notable photothermal therapy properties, close structural resemblance with biomolecules and the possibility of tethering various functional groups on the surface of CNTs promote their application for multimodal therapy, as carrier for therapeutics, in diagnosis, for prosthesis delivery, and as a matrix for fabricating tissue regeneration scaffolds [2–7]. Metal

nanoparticles (NPs) or quantum dot-conjugated CNTs have been used as labelling, imaging and tracking agents [2,8,9]. Folic acid and nucleic acid aptamers are examples of targeting moieties studied for cancer therapy that can bind specifically to target cells [10,11]. Antineoplastic drugs and biomolecules are used as therapeutic agents for various cancer treatments [12,13]. Polymers are used as a structural host matrix for CNTs, function as stealth or biocompatible coatings and are also used as carriers in drug delivery systems (DDSs) [3,14–16].

Despite the huge progress in the development of CNT-based biomedical components; cytotoxicity is a bottleneck preventing commercial exploitation [17]. Efforts have been made to assess cytotoxicity and to comprehensively enhance CNT biocompatibility. Cellular assays have been studied extensively using several cell types such as skin (HaCaT), lung (A549), pharynx (FaDu), blood-cell elements (macrophages), kidneys (HEK293) and disease-specific animal models such as human volunteers, rats, pigs, mice and rabbits [18–29]. Skin, lungs and blood-borne cells are relatively more challenging but are easily accessible organs in a given CNT-polluted environment [30]. Results are more specific to the type of cell line, assay, composition (preferably catalytic metal impurities), chemical structure and dimension of the CNT, including length, surface area and diameter [30]. Considerable attention has been paid to study the pulmonary effects of CNTs using lung-specific A549 cells [20–24,31]. Moreover, a variety of factors interfere with and alter results of *in vitro* cytotoxicity test systems, thereby the applicability of these systems has been scrutinized due to false-positive results [20]. Examples of systemic interference are adsorption of assay components such as fetal bovine serum, vitamins and CNT indicators [32], toxicity of surfactants [33] and the interaction of CNTs with colorimetric indicators such as assay dyes [19,20,23]. CNTs may adsorb assay ingredients resulting in a depletion of nutrients and a decrease in cell viability [32]. Consequently, reports on the cytotoxicity of CNTs appear contradictory, and there is a consensus among various research groups to obtain more insights on CNT toxicity for materials designed for biomedical applications [5,30].

Porter *et al*. [34] demonstrated the reliable non-toxic effect of carboxyl functionalized CNT for imaging and delivery application. With the acquired knowledge, the single-walled CNT (SWNT) was functionalized with carboxylic group, NPs, DNA and PVA to fabricate hybrid composite (HC). In addition, we sequentially studied the cytotoxicity of the nanomaterials (NMs) and hybrids obtained at various steps during formation of the HC. We designed our HC to mimic a theragnostic system that includes a carrier (SWNT)-imaging agent (AgNPs) and therapeutic agent (DNA)-encapsulating polymer (PVA). SWNT is widely used as a carrier in DDS [5,35]. AgNPs can be used as a Raman tag for imaging [36]. DNA can be used to represent the therapeutic agent (for genetic disorders) as well as a targeting moiety (nucleic acid based aptamers) [11,13]. PVA is a recognized biocompatible material that has been used for fabricating biomaterials, and hydrogel-based DDS for sustained release [37–39]. In particular, PVA is well known for its non-toxic, non-carcinogenic and bioadhesive properties [40]. We selected lung-specific A549 cells for our study, because pulmonary toxicity has substantially limited the applicability of CNTs [31]. Additionally, mouse fibroblast cells (NIH3T3) and human bone marrow stromal cells (hBMSC; HS-5) were used to speculate the tissue engineering and regenerative application of HC. Cytotoxicity was assessed and visualized by the CCK-8 assay and bioatomic force microscopy (bio-AFM) imaging, respectively. As a complementary study to AFM imaging, force spectra (FS) analysis was carried out for cells treated with materials to observe biophysical and biomechanical changes of cells before and after the treatment. Overall, this study attempts to unravel the material interactions with cells, the resulting cytotoxicity and cellular properties. Our findings demonstrate that materials composition such as metal impurities and surfactant exhibit toxicity that was substantially reduced by suitable functionalization. The toxicity of materials is linked with cellular properties, including roughness (R), adhesion force (AdF), attractive force (AtF), jump in to contact (DJC) and Young's modulus (YM) to open up new insights in the field of interface science.

2. Material and methods

Functionalization of NM and preparation of HC was carried out by using oxidation, *in situ* reduction and non-covalent interactions. Briefly, a strategy was developed to incorporate AgNPs into *c*-SWNT by *in situ* reduction under ultrasonication and to conjugate DNA via non-covalent bonding, which was further stabilized in a PVA polymer to be used as a multifunctional hybrid for biomedical applications [21]. Detailed experimental procedure, including materials, SWNT, carboxylation of SWNT (*c*-SWNT), incorporation of AgNPs on *c*-SWNT (c-SWNT-AgNPs; henceforth called hybrid), wrapping DNA or PVA on the hybrid (henceforth called hybrid-DNA and hybrid-PVA, respectively), functionalization of the hybrid-DNA with PVA as HC (*c*-SWNT-AgNPs-DNA-PVA; henceforth called HC), schematic illustration, morphological characterization, zeta potential measurements, determination of metal contents by inductively coupled plasma-mass spectroscopy (ICP-MS), cell culture, cytotoxicity (CCK-8 assay), glutathione (GSH) assay, evaluation of lipid peroxidation (LPO), cell transfection, biomechanics analysis of cells by AFM, force–distance curve measurement, surface roughness analysis and statistics are given in the electronic supplementary material S2.

3. Results and discussions

3.1. Cytotoxicity

Figure 1*a–c* illustrates viability of A549, NIH3T3 and HS-5 cells treated with the materials, respectively. The serially diluted samples were used for CCK-8 study, and the obtained data are provided in figure 1 (control, 40, 10 and 2.5 $\mu g\ ml^{-1}$) and in the supplementary material (table S1*a* for A549 cells). Cell viability was almost unaffected up to 2.5 $\mu g\ ml^{-1}$, irrespective of material composition, and the results agree with the previous report, particularly for *c*-SWNT [34]. Considerable changes in the cell viability started to appear at 10 $\mu g\ ml^{-1}$. The overall trend in A549 cell viability was in the following order: HC > hybrid > *c*-SWNT > hybrid-PVA > hybrid-DNA > SWNT. The highest (95% or more) and lowest cell viability (40% or less) at the highest dosage was exhibited by HC and SWNT, respectively. SWNT showed less than 40% viability at 40 $\mu g\ ml^{-1}$ dosage in A549 cells, and the toxicity exhibited by SWNT may have been due to the presence of impurities such as the metal catalysts used during SWNT synthesis. The metal impurities in the SWNT produce reactive oxygen species (ROS), oxidative stress and plasma membrane damage

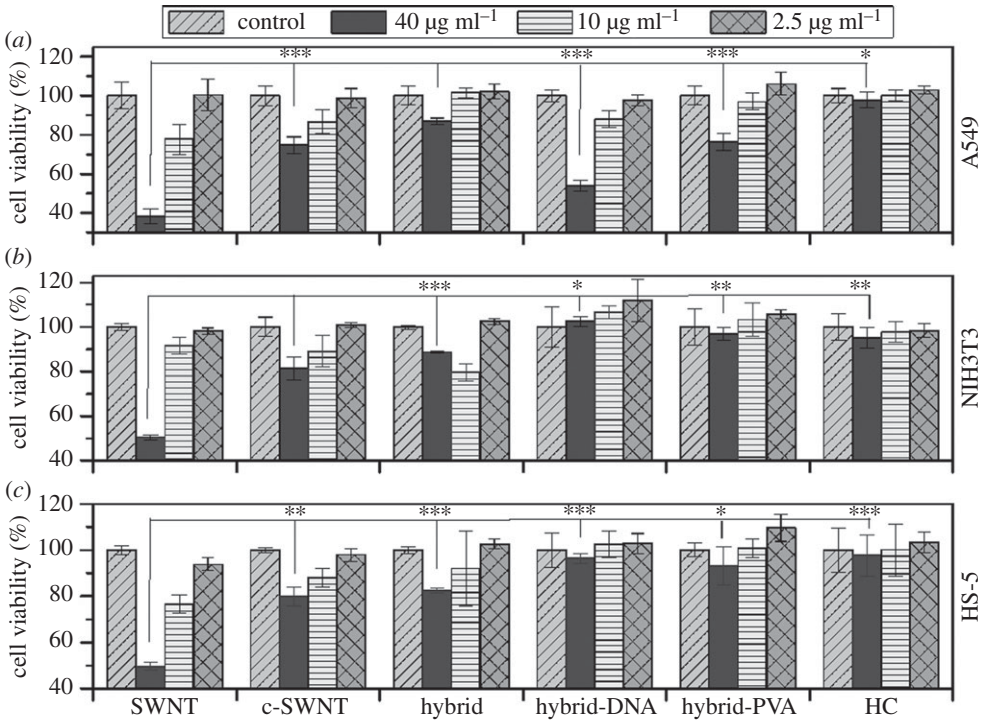

Figure 1. Toxicity assay. Cytotoxicity of sequentially functionalized materials in (*a*) A549 cells, (*b*) NIH3T3 cells, and (*c*) HS-5 cells evaluated by CCK-8 assay. The experiment was performed using serially diluted concentration. The colour indicates the concentration of materials in the graphs. Experiments were repeated seven times, and the significant difference between SWNT and the other hybrid is marked as $*p < 0.05$ or $**p < 0.01$ or $***p < 0.001$.

followed by rupture, disruption of metabolic pathways and cell death (figure 2*a*) [18]. *c*-SWNT toxicity was minimized due to the removal of catalytic metal impurities [34]. ICP-MS analysis (see electronic supplementary material, figure S3) confirmed a reduction in the quantity of metal impurities, such as Fe, Co, Ni and Mo after carboxylation. As a result, the quantity of Fe, Co, Ni and Mo decreased from 4995.6, 2849.9, 4556.7 and 6006.6 to 583.8, 352, 1006.4 and 521.4 $\mu g\ kg^{-1}$, respectively. The anionic surfactant (sodium dodecyl sulfate, SDS) could enhance the homogeneous dispersion and transfection of materials into the cells. The toxicity of SDS-treated hybrid was also tested, and the results show decreased A549 cell viability, irrespective of final material composition (see electronic supplementary material, figure S1*a*). The toxicity of the hybrid-SDS may have resulted from the usual toxic potential of the added anionic surfactant. In addition, the bare AgNPs displayed moderate toxicity which resulted from Ag^{+} ions and free radicals possibly interacting with disulfide or sulfhydryl groups of cellular enzymes to disrupt metabolic processes, followed by cell death (figure 2*a* and electronic supplementary material, figure S1*a*) [18]. The covalent conjugations of moderate toxic AgNPs on *c*-SWNT have altered the physico-chemical properties of hybrid such as neutral surface charge, increased size, minimized silver ion leaching and hence display better A549 cell viability. The hybrid-DNA shows reduced A549 cell viability, which explains anti-cancer activity of the hybrid material. In addition, an additional PVA coating (HC) stabilized A549 cell viability in the hybrid-DNA by greater than 95% even at the highest dosage. Hybrid-PVA was prepared to test the ability of PVA to form a stealth layer, which makes the hybrid system biocompatible. The cell-supportive behaviour of PVA was clearly ascertained by the A549 cell viability of the hybrid, mainly at the dosage limit of 2.5–40 $\mu g\ ml^{-1}$, which indicates that the PVA molecule acts as a contact point for the cell. Therefore, the biocompatibility showed by the PVA was not surprising. By contrast, wrapping DNA with the use of SDS resulted in an abrupt reduction in cell viability, which may have been due to the SDS surfactant used to disperse hybrid during DNA attachment (see electronic supplementary material, figure S1*a*) [33]. It is very important to emphasize that the common problem of interference of CNT with the assay indicator formazan did not influence the cytotoxicity results presented above [20,34].

Evaluation of GSH and malondialdehyde (MDA) was carried out to analyse the oxidative stress induced by materials in A549 cells. Intracellular total GSH levels in A549 cells displayed a dose-dependent decrease after 24 h exposure to materials (see electronic supplementary material, table S1*b*). The results indicate that exposure of A549 cells to the various materials altered the total GSH level plausibly. Hybrid containing SDS and SWNT induced the most significant reduction of the total GSH level by three- and fourfold that of the control group, respectively. The overall trend in depleted total GSH level was in the following order: hybrid-SDS-DNA (0.3 nM) > SWNT (0.4 nM) > hybrid-SDS (0.7 nM) > hybrid-DNA (0.6 nM) > *c*-SWNT (1.1 nM) > AgNPs (1.5 nM) > hybrid-PVA (1.6 nM) > hybrid (2.1 nM) > HC (2.9 nM). The amount of reduced GSH level is higher at 40 $\mu g\ ml^{-1}$, and this could be derived from reduction of GSSG by glutathione reductase via a conjugation reaction that led to intracellular activity (figure 2*a*). The production of MDA, an indicator of LPO, confirms the oxidative stress environment in cells. MDA concentration was measured to elucidate the induced intracellular LPO levels in A549 cells after 24 h exposure to materials. The results have demonstrated a dose-dependent increase in total LPO (figure 1*c* and electronic supplementary material, table S1*c*). *c*-SWNT, hybrid-SDS, hybrid-DNA samples treatment at 40 $\mu g\ ml^{-1}$ have shown

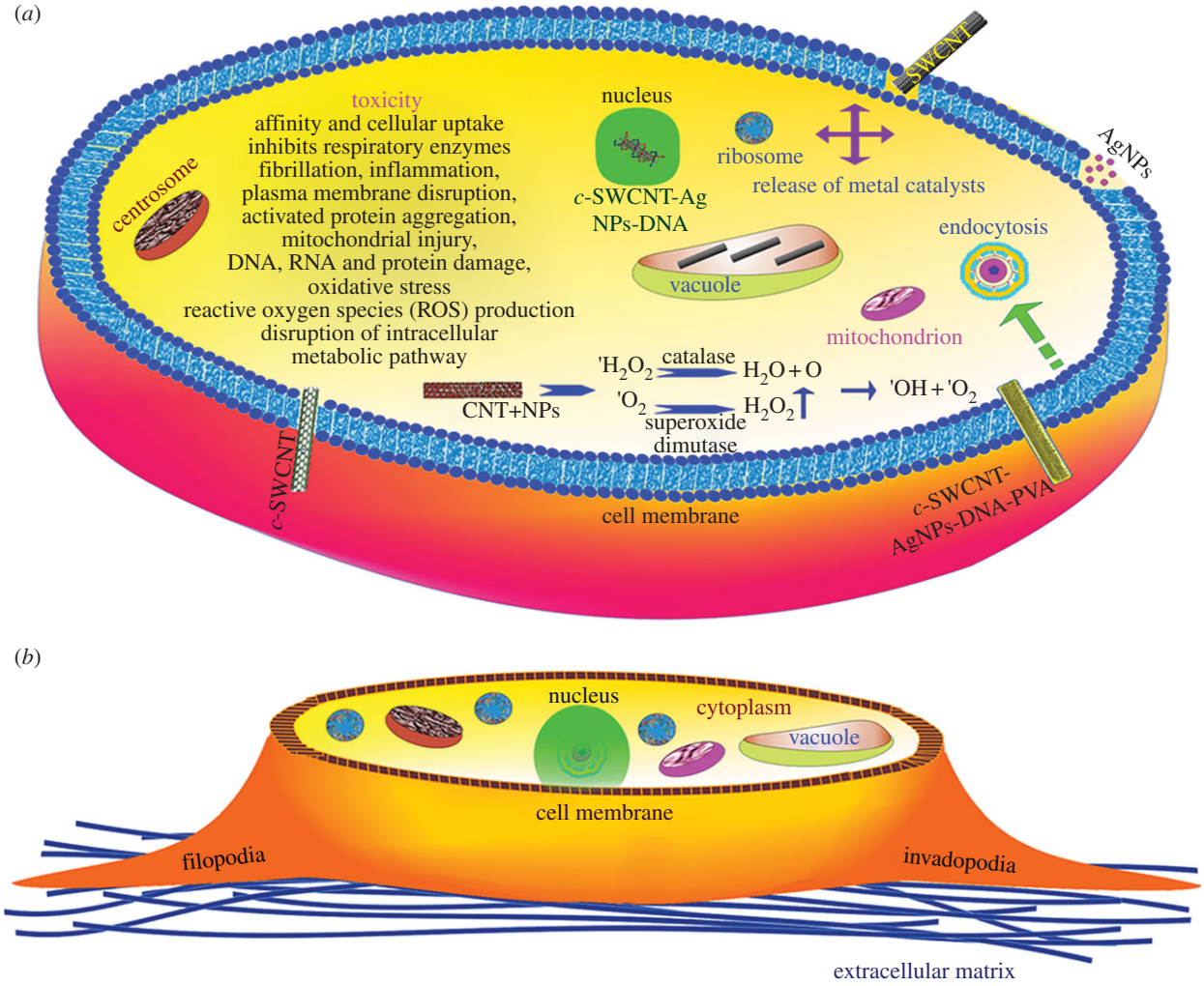

Figure 2. Schematic of a cell structure and material toxicity mechanism. (*a*) The toxicity exhibited by materials and (*b*) structure of cell is schematically illustrated. Specialized outgrowth cellular structures called invadopodia can be seen in the A549 cells that differentiates them from normal lung cells that enhance the carcinoma cell invasion. Similar structures called filopodia can be seen in NIH3T3 and HS-5 cells. The biophysical and biomechanical analysis was carried out in the cytoplasmic and perinuclear region of cells.

increased MDA production by three, 2.5 and fourfold the level of the control, respectively. The increased LPO levels can be stratified as follows: HC > hybrid > AgNPs > hybrid-PVA > *c*-SWNT > hybrid-DNA > hybrid-SDS > SWNT > hybrid-SDS-DNA. Importantly, SWNT and hybrid-SDS-DNA exhibited an increased dose-dependent GSH depletion and MDA generation owing to the amplified metal ion release from SWNT, Ag^{+} ions and surfactant that induce the oxidant-free radical formation (figure 2*a*). The results clearly indicate that the MDA level is directly proportional to cell viability and GSH depletion and coincide well with each other. The overall results demonstrated that materials with metal impurities, SDS and moderate Ag^{+} ions released at dosage levels of 40 and 10 $\mu g\ ml^{-1}$ can induce significant intracellular oxidative stress that causes the cell death. According to the results of A549 cell viability, the following samples (i) SWNT, (ii) *c*-SWNT, (iii) hybrid, (iv) hybrid-DNA, (v) hybrid-PVA, and (vi) HC were also evaluated for their toxic potential in NIH3T3 and HS-5 cells and require further research. The very similar A549 cell viability trend was experienced in NIH3T3 and HS-5 cells except for hybrid-DNA. The viability of NIH3T3 and HS-5 cells coincides with A549 cells except hybrid-DNA, and the overall trend can be listed as follows: HC > hybrid-DNA > hybrid-PVA > hybrid > *c*-SWNT > SWNT. Hybrid with DNA, PVA and HC displayed better viability and demonstrates their potential application in tissue engineering and regenerative medicine.

3.2. Morphology

The morphology of the newly synthesized materials was studied to better understand the influence of materials on cell structure. Figure 3 depicts the FE-SEM, AFM and HR-TEM images of (*a*) SWNT, (*b*) *c*-SWNT, (*c*) hybrid, (*d*) hybrid-DNA, (*e*) hybrid-PVA, and (*f*) HC. A slightly rough surface and aggregation were noted on the bare SWNT, whereas a smooth surface and homogeneous dispersion were noted with *c*-SWNT due to the high number of surface carboxyl groups. Notably, spherical-shaped AgNPs attached uniformly on the surface of *c*-SWNT (29.5 wt% loading of silver) after *in situ* functionalization (figure 3*c* and electronic supplementary material, figure S4). The cloudy appearance of the hybrid in figure 3*d* indicates that DNA was evenly wrapped, and a white coating of PVA was observed (figure 3*e*). Moreover, the visible bright spherical spot on the nanotubes showed strong incorporation of the AgNPs with *c*-SWNT and that its structure was maintained with high adhesion of DNA and the PVA coating (figure 3*c*–*e*). All three characteristic images obtained from FE-SEM, AFM and HR-TEM agreed with each other, and the size of

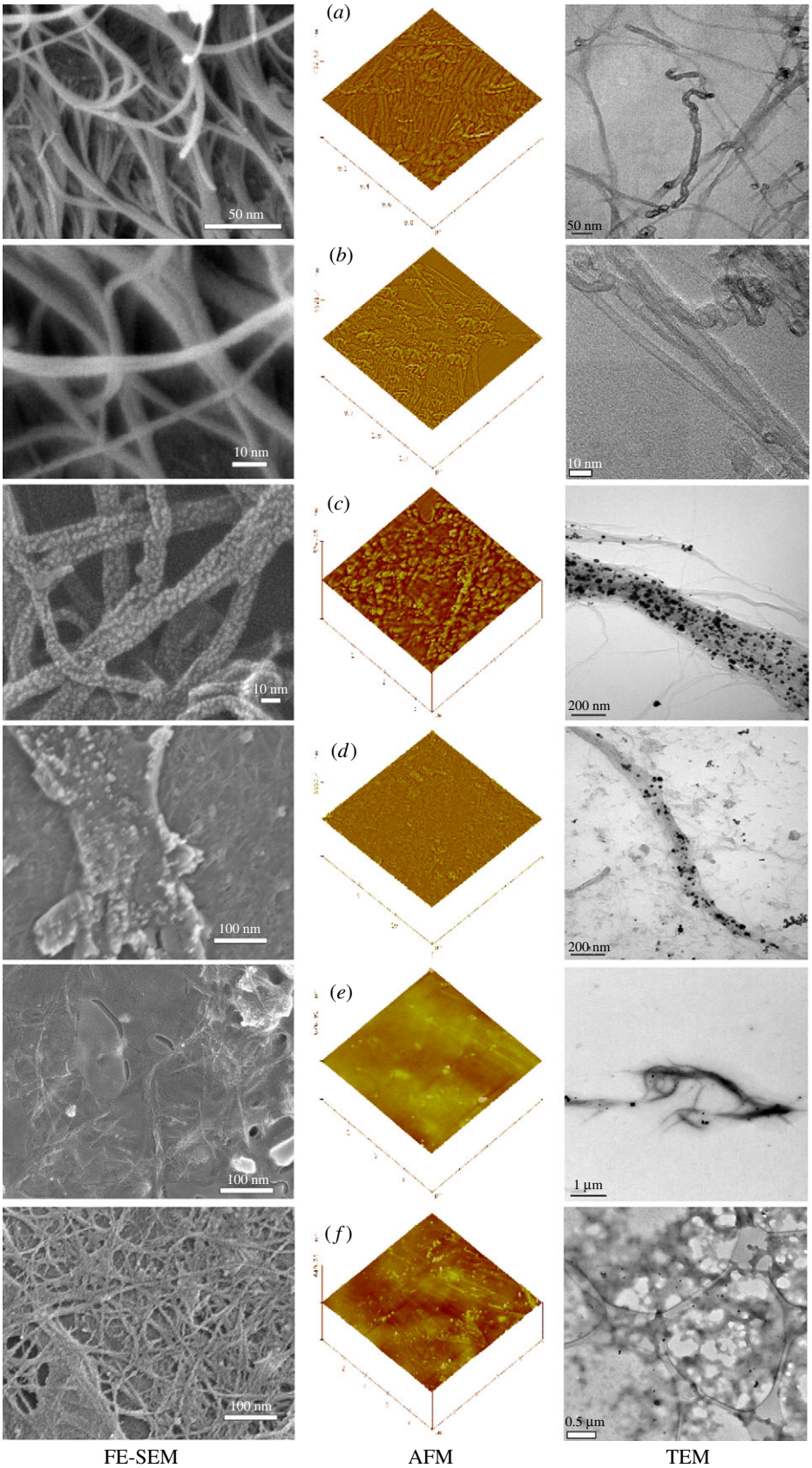

Figure 3. Materials morphology. FE-SEM, bio-AFM and TEM images of (*a*) SWNT, (*b*) *c*-SWNT, (*c*) hybrid, (*d*) hybrid-DNA, (*e*) hybrid-PVA, and (*f*) HC.

materials was evaluated and shown in table 1. The AgNPs were incorporated well with material covering and a one-dimensional structure. Unlike particulate accumulation from dispersion, the molecular covering from solution, i.e. DNA and PVA, was not significantly influenced by the size of the NM. This phenomenon may evince the molecular-level distribution of DNA, and PVA on the respective hybrid formed in the sequence. Disappearance of AgNPs on the PVA-coated hybrid confirmed the possibility that the PVA coating functions as a contact point for the entire NM in which it was incorporated (figure 3*e*,*f*). This PVA stealth layer might enhance cell viability by hindering any harmful

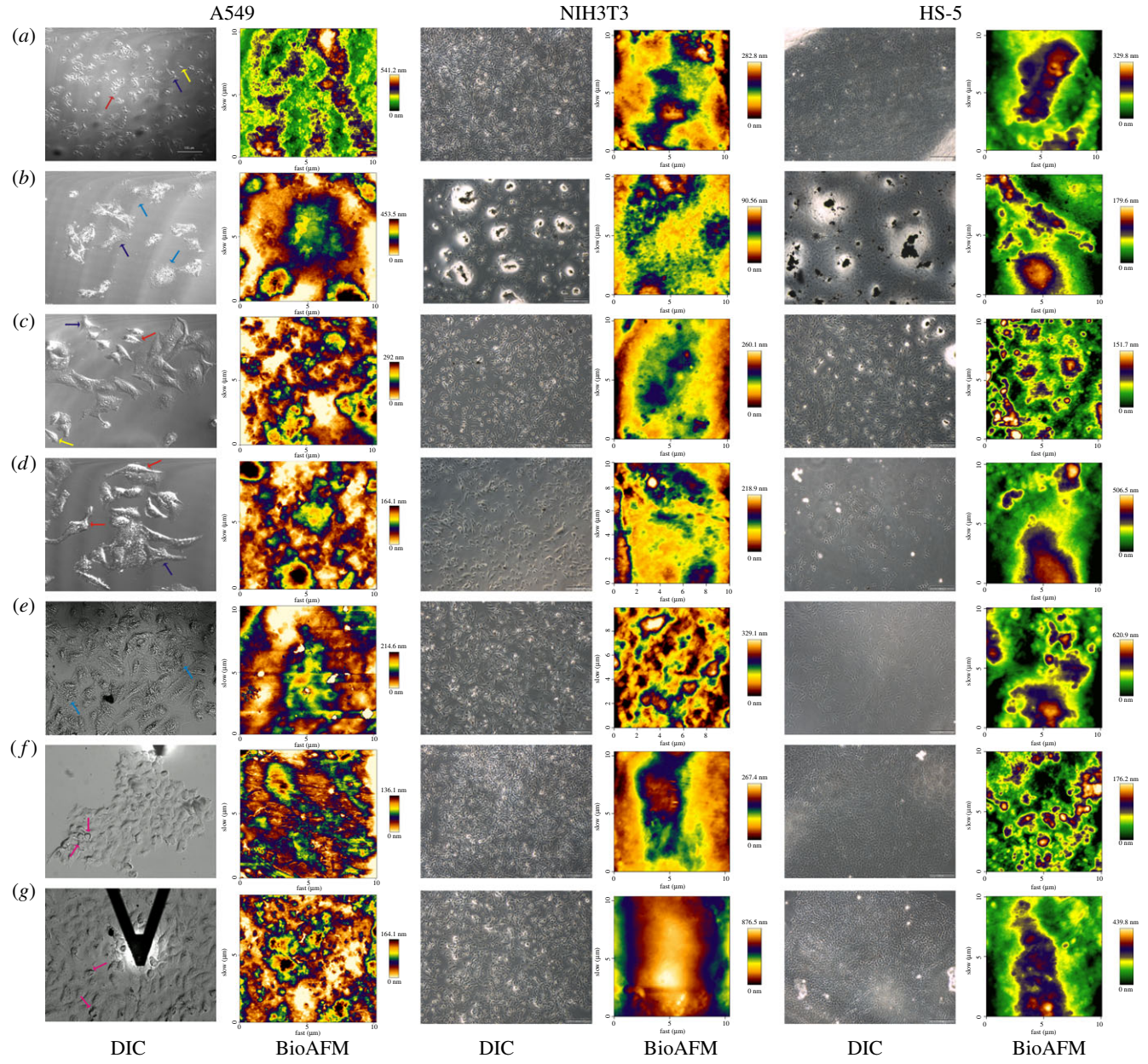

Figure 4. Morphology of cells treated with materials. Optical DIC images (scale bar, 100 µm), and bio-AFM height images (10 × 10 µm) of (*a*) cells, (*b*) cells + SWNT, (*c*) cells + *c*-SWNT, (*d*) cells + hybrid, (*e*) cells + hybrid-DNA, (*f*) cells + hybrid-PVA, and (*g*) cells + HC.

Table 1. Morphological parameters of materials.

			RMS roughness: R_q (nm)					cell height (µm)		
serial no.	samples	size (nm)	NMs, hybrid	A549	NIH3T3	HS-5	adhesion pattern of cells	A549	NIH3T3	HS-5
1	bare cells			156.5	109.8	121.9	stretched	1.4	1.1	0.8
2	SWNT	18 ± 5	6.6	132.6	51.0	87.2	cluster	1.3	1.4	1.4
3	*c*-SWNT	18 ± 5	5.7	285.1	67.2	148.9	stretched	1.4	1.1	1.2
4	hybrid	22 ± 6	35.0	258.2	73.8	234.2	stretched	1.6	1.1	1.2
5	hybrid-DNA	22 ± 6	18.9	208	147.0	254.5	cluster	0.9	1.7	3.1
6	hybrid-PVA	22 ± 6	2.9	269	73.9	137.0	cluster	3.4	1.1	1.3
7	HC	22 ± 6	3.7	217.5	51.7	139.5	cluster	1.5	1.0	1.6

species leached or produced from other participants in the hybrid that could degrade the cell, such as ROS from CNTs and Ag+ or free radicals from the AgNPs [24].

The materials exhibited considerable changes in roughness (table 1). Hybrid and hybrid-PVA showed the highest (35.04 nm) and lowest (2.09 nm) roughness, respectively.

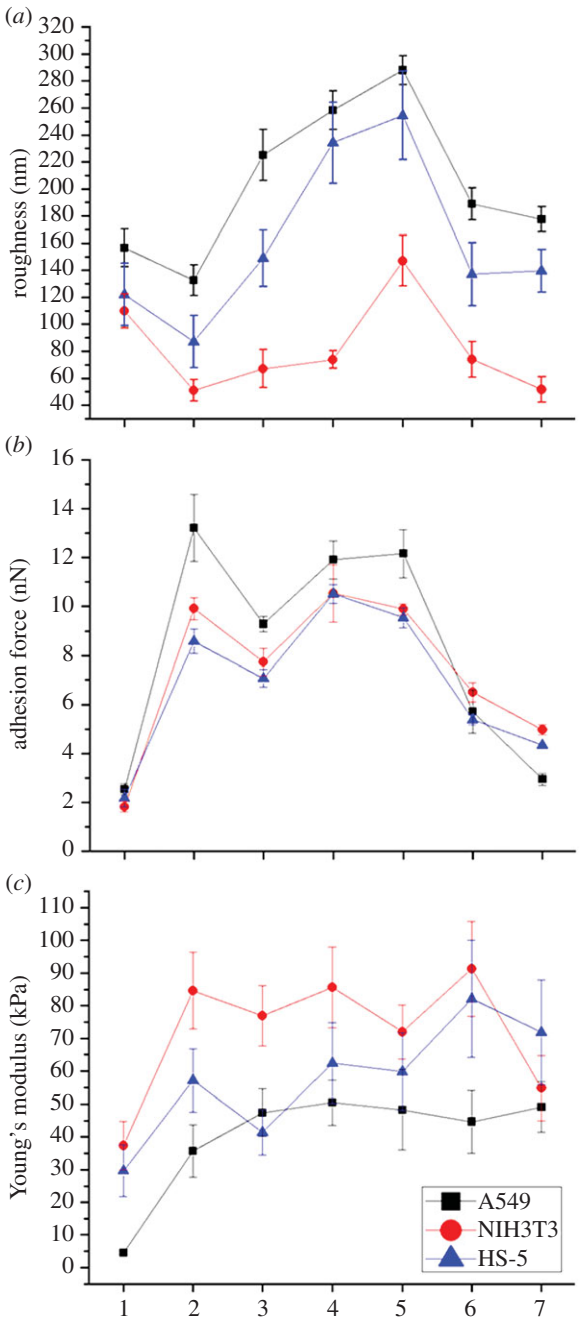

Figure 5. Roughness, adhesion force and Young's modulus of cells treated with materials. (*a*) Line graphs depict the roughness value, (*b*) adhesion force, and (*c*) Young's modulus measured in the cytoplasmic regions for the corresponding samples of (1) cells, (2) cells + SWNT, (3) cells + *c*-SWNT, (4) cells + hybrid, (5) cells + hybrid-DNA, (6) cells + hybrid-PVA and (7) cells + HC. Black, red and blue colour of line graph represents A549, NIH3T3 and HS-5 cells, respectively. The scanning region for roughness measurement was 20 µm in 10 different cytoplasmic regions of the cells. Young's modulus measured in the perinuclear region of the cells.

The carboxyl functionalization of the CNTs decreased the roughness by approximately 1 nm due to removal of amorphous carbon and the catalytic particulate impurities that adhered on the surface (see electronic supplementary material, figure S3). The roughness data indicate that adding AgNPs resulted in increased roughness, whereas PVA abruptly decreased it to yield a smooth surface. Similarly, DNA also had a notable impact on roughness. The highest roughness of hybrid was associated with the random distribution of AgNPs on the surface of *c*-SWNT. These morphological features demonstrate sequential formation of the materials and coincide well with our previous report [24].

The morphology of cells treated with 10 µg ml^{-1} of material on a glass coverslip was assessed by optical microscopy and bio-AFM. The best cell candidates were identified by optical microscopy and then scanned by bio-AFM to evaluate detailed topographic parameters. Figure 4 shows the differential interference contrast (DIC) and height images of material-treated cells captured by bio-AFM. Individual A549, NIH3T3 and HS-5 control cells were uniformly distributed over the substrate surface (figures 4*a* and 8). Groups of cell were found, but there were no clusters. The A549 cells exhibited their characteristic shape, most importantly, the appearance of invadopodias, which are actin-rich membrane protein protrusions of cancer cells that contribute to tissue invasion through the degradation of extracellular matrix and are responsible for metastasis (figures 2*b* and 8*a*) [41]. Approximately 70% of human lung carcinoma cells are bipolar but 30% contain one, three or more invadopodia, which are indicated by arrows in the optical images (figure 4, A549) [41]. The control specimen showed all possible shapes of mono-, bi- and tri-polar cells, and bi- and tri-polar cells were dominant. Circular objects with detectable and poor contrast may represent non-fixed and dead cells that are floating on the surface. Circular shapes with detectable contrast may also indicate shrunken and non-fixed cellular objects or water-insoluble crystals (figure 4). A similar trend was noted in material-treated NIH3T3 and HS-5 cells. The SWNT-treated specimen showed many circular objects varying in contrast, which may be very small cellular material (figure 4*b*). Besides the few mono- and di-polar cellular bodies, the rough and cluster-like objects found may represent debris. Aggregated SWNT was found as accumulation on the surface of NIH3T3 and HS-5 cells, and such mass was absent in *c*-SWNT-treated cells, indicating excellent dispersion of *c*-SWNT (figure 4*b*,*c*). Similar to SWNT, the *c*-SWNT treatment also produced a relatively small number of circular objects with poor contrast and few large bipolar intrinsic cells with a very rough surface. Few bi- and tri-polar cells, circular objects with poor contrast, and islands and aggregates with diffused layer-like rough surfaces were found in the hybrid-treated specimen. These layer-like objects were consistent with disintegrated cell membranes caused by internalization of hybrid, because cells will hold their original shape during adhesion, but the magnitude of roughness was similar. The DIC image of hybrid-DNA-treated specimens also showed cells with very rough surfaces and disintegrated membranes (figure 4*e*, A549). These results reflected the moderate cell viability observed for specimens treated with hybrid-DNA. In contrast with these specimens, PVA incorporated hybrid exhibited individual but connected layer-like morphology, and A549 shaped structures with or without very small invadopodia. In the case of NIH3T3 and HS-5 cells, the hybrid-PVA and HC acts as a two-dimensional scaffold, and treated cells exhibited similar morphology and homogeneous arrangement (figure 4*f*,*g*). The triangular object seen in the image (figure 4*g*, A549) is the AFM tip. The population and height of the cells treated with hybrid containing PVA appeared higher than those of cells treated by other materials. The morphology of the materials-treated specimens correlated well with the cytotoxicity data.

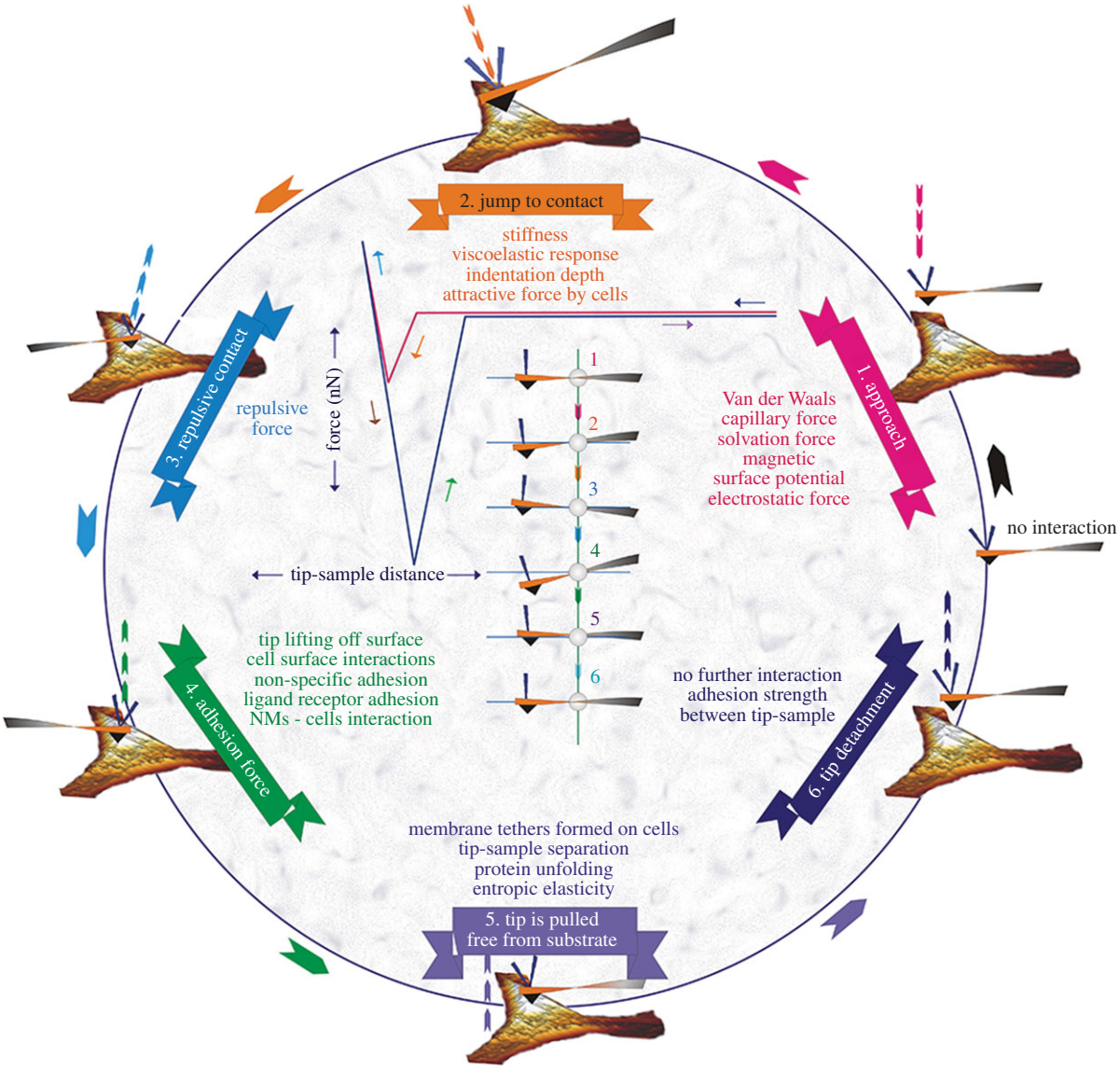

Figure 6. Schematic of AFM-force spectroscopy operational principles. Schematic of the mechanism and process involved in force spectroscopy starting from tip approach, jump into contact, repulsive contact, adhesion force, tip release and detachment from surface. Corresponding tip angle and forces involved on each step are also graphically demonstrated (correlate the title colour with serial numbers and force curve in the image; also see table 2).

Table 2. Possible interactions between Si_3N_4 tip and materials.

serial no.	interaction	possible interaction
1	tip and glass	dipole–dipole, capillary and salvation forces due to adsorbed water
2	tip and SWNT	dipole-induced dipole
3	tip and *c*-SWNT	ion–dipole, capillary and salvation forces due to adsorbed water
4	tip and *c*-SWNT-AgNPs	ion–dipole, capillary and salvation forces due to adsorbed water
5	tip and *c*-SWNT-AgNPs-DNA	ion–dipole, capillary and salvation forces due to adsorbed water
6	tip and *c*-SWNT-AgNPs-PVA	dipole–dipole, capillary and salvation forces due to adsorbed water
7	tip and *c*-SWNT-AgNPs-DNA-PVA	dipole–dipole, capillary and salvation forces due to adsorbed water

Bio-AFM images in figure 4 show the topography of representative single-cell candidates (10×10 μm) treated by the materials. The topographic images confirmed the shape of the cells captured by optical microscopy (figures 4 and 8). The nature of the cell surface, dimensions and height can be directly determined from these images. Overall, two different cell attachment patterns were found, such as stretched and diffused clusters. The control, *c*-SWNT and hybrid-treated cells followed the former, and the others followed the latter. Consequently, as shown in table 1, cells with stretched and diffused cluster

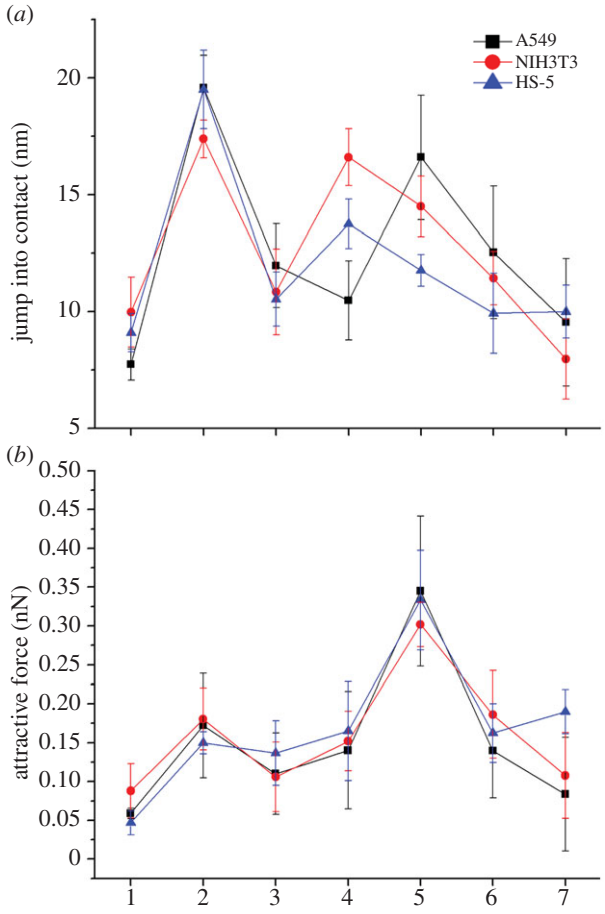

Figure 7. DJC and AtF of cells treated with materials. Line graphs depict the distance at which the tip (*a*) jumped into contact, and (*b*) attractive force obtained from the FS of corresponding samples (1) cells, (2) cells + SWNT, (3) cells + *c*-SWNT, (4) cells + hybrid, (5) cells + hybrid-DNA, (6) cells + hybrid-PVA and (7) cells + HC. Black, red and blue colour of line graph represents A549, NIH3T3 and HS-5 cells, respectively. FS obtained for the materials are given in electronic supplementary material, table S2.

patterns exhibited different height profile according to the hybrid–cells interaction. Furthermore, the R_{rms} of the cell surface was evaluated and listed in table 1 and figure 5*a* to describe the nature of the cell surface statistically. Two different regions on the cell surface (figure 2*b*), possibly representing invadopodia and cytoplasm, were selected for the roughness study in A549 cells. In both control- and sample-treated cells, the trend in roughness followed the order of invadopodia < cytoplasm (see electronic supplementary material, figure S5). In a previous report, the centre part of the A549 cell was described as smoother than the edge, therein the centre part of the image was brighter, and the surface was not clearly visible, but no roughness data were provided [41]. The control- and HC-treated cells showed roughness around the invadopodia at close range, and it was at least doubled in other specimens. Notably, hybrid-DNA showed closer to a fourfold increase when compared with the control. This result indicates adherence of materials to the invadopodia when correlated with the roughness data (figure 5 and electronic supplementary material, figure S5). The PVA-coated hybrid, which may be internalized, may show restricted growth of invadopodia as seen in figure 4*f*,*g* (see electronic supplementary material, figure S5). In other words, the robust coverage of the PVA-coated hybrid may also mechanically restrict the growth of invadopodia. Hybrid-PVA among the entire synthesized materials has drastically reduced the roughness in the invadopodia region that claims active arrest of invadopodia growth thereby preventing cell–cell interaction and simultaneous proliferation (figure 4*f*,*g*). A considerably different trend was observed in the cytoplasm. A549 cells treated with SWNT, *c*-SWNT and hybrid-DNA showed roughness values close to the control, and these materials may not adhere to this part of the cell. Hybrid and hybrid-PVA resulted in the lowest and highest roughness, respectively. Hybrid-PVA may alter the cell surface and may cause higher roughness. The lowest roughness was shown by the SWNT-treated cells in the cytoplasm region. Except for SWNT, the hybrid resulted in at least a half-fold increase in roughness at the surface representing the nucleus. SWNT showed roughness slightly lower than that of the control and it might not have adhered to this part. The increase in the roughness of cells treated with other materials may be due to the modification caused on the cell surface because of adherence or internalization. Hybrid-DNA and SWNT-treated NIH3T3 and HS-5 cells have shown higher and lower roughness, respectively. Hybrid-PVA and HC have minimized the cell roughness which indicates the layer formation of PVA on cell surface.

3.3. Force spectroscopy

Force spectroscopy is widely known as a viable tool for probing the surface of nanostructured architecture, including label-free imaging of cells in their native environment [42–44]. The application modes of AFM such as electrostatic force microscopy, piezo-response force microscopy, scanning thermal microscopy, near-field scanning optical microscopy and phase detection microscopy are well explored in materials science research [45]. Force spectroscopy is a unique application that has upgraded AFM as a tool that best suits biological studies [46]. The unique point of force spectroscopy is the spanning direction of the cantilever during surface probing. The interfacial interactive forces come into effect when the tip is approaching the sample. The short- and long-range attractive forces and physiochemical sensitive adhesion forces control the tip–sample interaction depending on the distance, and allow the cantilever to deflect naturally (figure 6). As a result, measurements of interactive forces allow us to assess the mechanical properties of the nanostructured/biological material. Furthermore, the nature of the interaction between specific molecules can be elucidated by attaching a target molecule to the tip. The detailed operation principle and applications of FS are well documented [44–48].

Figure 6 schematically represents FS in which region-specific forces are indicated. FS were performed at a minimum of 10 different places on the specimen surface. Representative FS of materials and treated cells are shown in the electronic supplementary material, figure S6 and S7, respectively. FS of specimens were characterized in terms of distance at which the tip jumped in contact (DJC) with the specimen, extent of attractive (AtF) and adhesion (AdF) forces exerted between the tip and specimen. These parameters will be discussed in sequence. The data were analysed using Student's *t*-test, and the average values of the parameters of interest were calculated for materials and treated cells and are provided in the electronic supplementary material, table S2 to reach insights regarding the nature of the competitive interaction between the tip–cell and materials–cell. The surface charge of the materials was assessed by zeta potential measurements in an aqueous medium at pH 7,

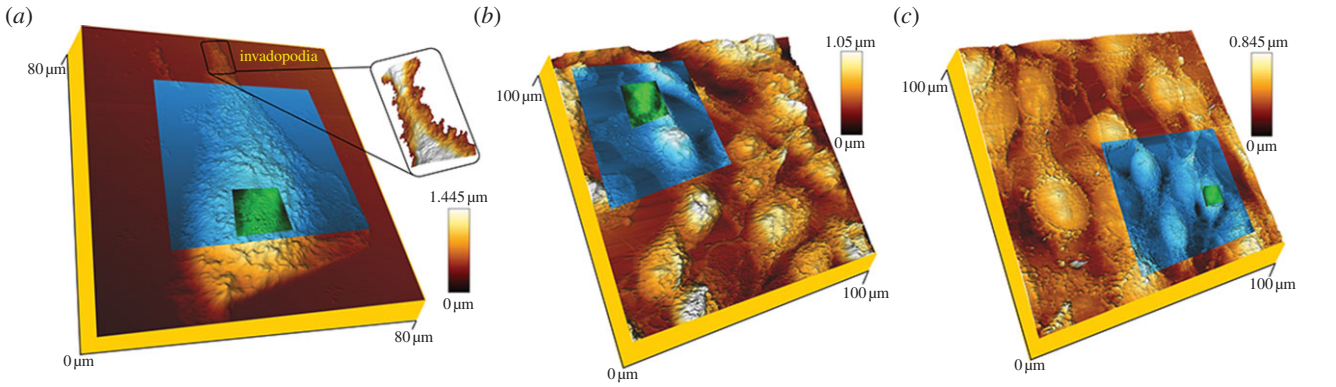

Figure 8. Bio-AFM three-dimensional height images of cells for biomechanics and biophysical analysis. AFM three-dimensional image of (*a*) A549, (*b*) NIH3T3 and (*c*) HS-5 cells scanned in an order of 80 × 80/100 × 100 µm (dark gold), 60 × 60/50 × 50 µm (light blue) and 10 × 10 µm (fluorescence green) scale. The typical bipolar structure of strong proliferative invadopodia is pictured and shown as an extension image (inset). The 10 × 10 µm scale green image represents the central region of the cells which is used for the stiffness measurement.

and the respective electrical potential graph is provided in the electronic supplementary material (figure S8). The surface charges (mV) of the materials were SWNT = 0.14, *c*-SWNT = −62.3, *c*-SWNT-AgNPs = −0.46, *c*-SWNT-AgNPs-DNA = −43.5, *c*-SWNT-AgNPs-PVA = −0.003 and *c*-SWNT-AgNPs-DNA-PVA = −29.7.

Similarities between FS of materials and treated A549 cells were observed (see electronic supplementary material, figures S5 and S6). The tip encountered short-range attractive forces upon approach and a wide adhesion peak upon retraction. The tip jumped into contact from distances of 5–220 nm, indicating short-range attractions between the tip and samples. It is well documented that the tip will experience short-range attractive forces from nanometre approaches to atomic distances, long-range attractive forces start to become an influence at a few micrometres of distance. Electrostatic forces are the dominant long-range interactive forces in the case of materials. Van der Waals forces, capillary forces, Derjaguin, Landau, Verwey and Overbeek forces/screened electrostatics, magnetic interaction and solvation forces are possible short-range interactive forces [44–48] that the tip could experience at the interface region. Thus, nanometre range DJC reveals the absence of long-range attraction between the tip and samples and treated cells. A clear difference in DJC can be seen upon sequential functionalization of materials (figure 7*a* and electronic supplementary material, table S2). The DJC was almost two to four orders of magnitude higher for *c*-SWNT and SWNT than that for the glass substrate, and reached 10.48 ± 2.69 nm when AgNPs attached *in situ* on the *c*-SWNT surface, then increased to 16.6 ± 2.66 nm when DNA was added. A profound decrease in DJC was observed upon PVA coating on the hybrid and hybrid-DNA; the decrease was very high for the former. A very similar DJC profile was also noted for NIH3T3 and HS-5 cells treated with all samples except hybrid and HC. An abrupt change in DJC was observed for both control and cells treated with samples, particularly the materials-treated A549 cells showed a moderately higher DJC than control cells (figure 7*a*). DJC values differed by almost one to three orders of magnitude for cells treated with materials when compared with control.

Figure 7*a*,*b* shows a graphical representation of the DJC and AtF values obtained from FS for the materials and treated cells, respectively (see electronic supplementary material, table S2). Notable variations can be seen in the AtF values for the materials, starting from bare glass in which AtF increased gradually (see electronic supplementary material, figure S6*a*). Adding AgNPs resulted in a peak at 2.63 ± 0.08 nN (see electronic supplementary material, figure S6*e*). DNA incorporation resulted in a decrease of AtF to 0.62 ± 0.16 nN, and PVA coating further decreased the AtF, irrespective of materials composition (see electronic supplementary material, figure S6*f*–*h*). By contrast, the AtF between the tip- and materials-treated cells increased steadily from the control to DNA incorporation, but PVA coating decreased AtF in the same manner as shown for the bare materials. As AtF mainly originates from surface chemistry excluding physical structure-dependent interactions such as capillary forces, it is better to analyse the nature and strength of attractive forces exerted between the tip–materials, –cells and –materials. Possible attractive forces that dominate the tip–samples interaction were predicted and are listed in table 2. Accordingly, the higher DJC shown (see electronic supplementary material, table S2) by the hybrid can be attributed to a strong intermolecular interaction with the tip compared with that between the materials themselves, which was confirmed by the largest AtF shown by hybrid. These materials possesses a very small negative charge on the surface; thus, the role of dipole–dipole and ion–dipole interactions was low, and solvation forces due to water molecules adsorbed both on the tip and on the surface of the materials together with capillary forces were probably responsible for the higher AtF. The lower AtF shown by the materials with a higher negative charge and SWNT can be explained by the lower contribution of ion–dipole, dipole–dipole and dipole-induced dipole-type interactions to the AtF values observed between the materials and tip. In other words, the highest AtF may be due to the least interaction between the materials themselves.

The relatively lower DJC and AtF shown by the control and cells treated with materials indicates that the interaction between the hydrophilic tip and hydrophobic cell membrane was weak, or that the interaction between cellular membrane components was high, and the integrity of the cell membrane might remain intact. The reason for the higher DJC (figure 7*a*) of the SWNT-treated cells could not be explained, because the presence of SWNT enhanced the hydrophobicity of the cell membrane so that it cannot strongly interact with the polar Si_3N_4 tip, as shown by the corresponding AtF value. A slightly higher AtF exhibited by cells treated with hybrid-DNA explains the possibility of an increase in cell membrane hydrophilicity, which can increase the magnitude of attraction

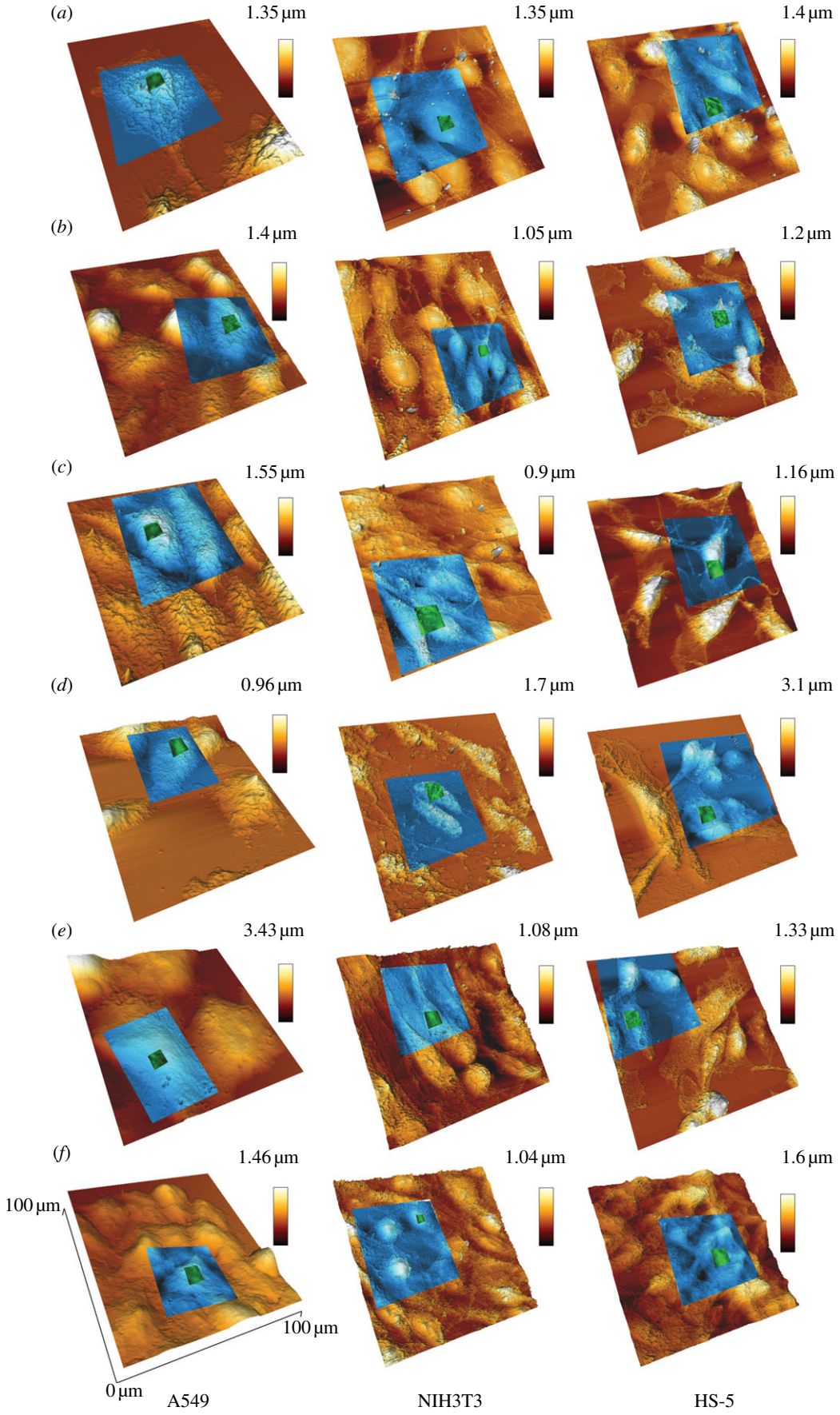

Figure 9. Bio-AFM three-dimensional height images of materials-treated cells for biomechanics and biophysical analysis. AFM three-dimensional images of (*a*) cells-SWNT, (*b*) cells-*c*-SWNT, (*c*) cells-*c*-SWNT-AgNPs, (*d*) cells-*c*-SWNT-AgNPs-DNA, (*e*) cells-*c*-SWNT-AgNPs-PVA and (*f*) cells-*c*-SWNT-AgNPs-DNA-PVA, respectively. Cells scanned in an order of 100 × 100 µm (dark gold), single cell (light blue) and centre region of the cell (fluorescence green-stiffness measured area), respectively.

with the polar tip. Similarly, a higher AtF can be expected between cells treated with polar PVA, provided they were just adsorbed on the cell membrane; however, it was actually rather less than or equal to the AtF corresponding to control. Here, the lower AtF observed for cells treated with PVA-coated hybrid indicates two possibilities: (i) these hybrids

might be internalized due to the biocompatible nature of PVA, and (ii) the hydrophilic PVA coating prevented adhesion of hybrid on the hydrophobic cell membrane.

Figure 5*b* shows a graphical representation of AdF values obtained from FS. Bare glass substrate, and SWNT showed AdF values closer to or less than 1 nN, but *c*-SWNT (9.23 $\pm$ 1.36 nN) and hybrid (5.21 $\pm$ 0.06 nN) were higher (electronic supplementary material, table S2). The PVA-coated hybrid showed AdF just above 2 nN. By contrast, materials-treated cells exhibited marginally higher AdF than that of the control (2.5 nN). AdF increased highly for cells-SWNT, -hybrid and -DNA with slight variation. An abrupt decrease in AdF was observed in cells treated with hybrid-PVA and HC but it was still an order of magnitude higher than that of the control, indicating the possibility of internalization of these materials into the cell membrane. The unique round morphology observed in the bio-AFM images of cells treated with the PVA-coated hybrid might have resulted from internalization.

3.4. Biomechanics

The nanoindentation analysis was performed using AFM software, and FS were measured consecutively 100 times at different positions on the central region of the cells surface (10 μm scale of green colour overlap image in figures 8 and 9). Three AFM scanning was separately carried out in an order of 80–100, 60 and 10 μm, respectively, and displayed as an overlapped single image in figures 8 and 9. The recorded AFM–FS curve was changed to tip–sample separation curve and fitting with the Hertz model using JPK software for measuring Young's modulus of cells. The biomechanical response of A549, NIH3T3 and HS-6 cells before and after treatment with materials (24 h; 10 μg ml^{-1} dosage) was assessed to investigate the role of hybrid on mechanical changes in cells. The average Young's modulus for untreated A549, NIH3T3 and HS-6 cells was found to be 4.5 $\pm$ 0.43, 37.3 $\pm$ 7.36, 29.6 $\pm$ 7.9 kPa ($n = 100$), respectively, whereas the stiffness of cells after treatment with materials increased drastically (figure 5*c*). The stiffness of A549 cells treated with SWNT, *c*-SWNT, hybrid, hybrid-DNA, hybrid-PVA and HC was found to be 35.6 $\pm$ 7.9, 47.7 $\pm$ 7.1, 50.4 $\pm$ 6.9, 48.3 $\pm$ 12.3, 44.6 $\pm$ 9.5, 49.03 $\pm$ 7.6 kPa ($n = 100$), for NIH3T3 was found to be 84.6 $\pm$ 11.7, 76.9 $\pm$ 9.2, 85.6 $\pm$ 12.4, 71.9 $\pm$ 8.3, 91.3 $\pm$ 14.4, 54.7 $\pm$ 9.9 kPa and for HS5 was found to be 57.1 $\pm$ 9.6, 41 $\pm$ 6.9, 62.4 $\pm$ 12.3, 59.8 $\pm$ 11.8, 82.1 $\pm$ 17.8, 71.8 $\pm$ 16 kPa, respectively. The results explicate that materials significantly increase the stiffness of A549 cells, irrespective of materials composition, suggesting a notable anti-proliferation activity of materials on the A549 cells [41]. NIH3T3 and HS-5 cells stiffness increased upon SWNT and hybrid treatment and decreased with *c*-SWNT, hybrid-DNA and HC, whereas hybrid-PVA-treated cells show elevated stiffness due to the polymer deposition on the surface of cells. The bare A549, NIH3T3 and HS-5 cells show long invadopodia and filopodia that accelerate cell proliferation, invasion and strong interaction with neighbouring cells with aforementioned mechanical stiffness of figures 4*a*, 5*c* and 8. But materials either strongly adhere to the cell surface or are translocated into the cells and generate a mechanical stress from the cell wall towards cytoplasm (figure 2). The accumulation and translocation of materials on the cell surface is generally considered for the elevation of stiffness in cells. Exceptionally, hybrid-PVA creates a thick coating on the surface of treated cells that arrests invadopodia/filopodia invasion, as a result the cells bulge due to the mechanical stress. The thick PVA layer is clearly seen in figures 4*f* and 9*e* with the average height of 3.4 (A549), 1.08 (NIH3T3) and 1.33 μm (HS-5). In addition, similar pattern is noted with HC (figures 4*g* and 9*f*).

4. Conclusions

DDS-mimicking HC consisting of tetrad materials were successfully prepared. Cell viability was altered as a function of hybrid formation, and the cytotoxicity results demonstrate that carboxylation and functionalization increase cell viability of NMs to a significant level. Optical microscope and bio-AFM studies showed that the hybrid treatment considerably changed cell morphology, and altered the formation of invadopodia/filopodia, which are decreased following treatment with the hybrid-PVA and HC. This result suggests that changes in cell metabolism occurred due to internalization or deposition of the materials. As a result Young's modulus of materials-treated cells increased significantly and evinced the biomechanical change of cells. In most cases, the roughness of the hybrid-treated cells increased. FS indicated a possible greater interaction between cells and materials and between cellular bodies. Cells treated with SWNT show higher toxicity, DJC and AdF. Hybrid-PVA and HC always exhibited distinct changes in the force curve; DJC, AtF and AdF were marginally lower than those of the other hybrid. These biophysical properties can be correlated with cellular behaviour to develop as a new biomarker. Although, several FS results could not be correlated well with the other analyses; the distribution of hybrid on or inside the cells will have to be studied in detail using confocal microscopy and cryo-transmission electron microscopy. Eventually, this study finding deserves future work and could be useful to develop theragnostic (concerted diagnosis and therapy)-based DDS for cancer treatment, i.e. safer internalization of materials that significantly affects cell metabolism with therapeutic significance.

Funding statement. This work was supported by grant no. 10032112 from the Regional Technology Innovation Programme of the Ministry of Knowledge Economy, Korean Ministry of Environment as 'Converging Technology Project' (191-101-001), Gachon University, Korea Institute of Science and Technology (KIST), and by the 2012 Research fund of the Ulsan National Institute of Science and Technology (UNIST).

References

1. Baughman RH, Zakhidov AA, de Heer WA. 2002 Carbon nanotubes: the route toward applications. *Science* **297**, 787–792. (doi:10.1126/science.1060928)
2. Saito N *et al*. 2009 Carbon nanotubes: biomaterial applications. *Chem. Soc. Rev.* **38**, 1897–1903. (doi:10.1039/B804822N)
3. Harrison BS, Atala A. 2007 Carbon nanotube applications for tissue engineering. *Biomaterials* **28**, 344–353. (doi:10.1016/j.biomaterials.2006.07.044)

4. Prato M, Kostarelcos K, Bianco A. 2008 Functionalized carbon nanotubes in drug design and discovery. *Accounts Chem. Res.* **41**, 60–68. (doi:10.1021/ar700089b)
5. Liu Z, Tabakman S, Welsher K, Dai H. 2009 Carbon nanotubes in biology and medicine: *in vitro* and *in vivo* detection, imaging and drug delivery. *Nano Res.* **2**, 85–120. (doi:10.1007/s12274-009-9009-8)
6. Lee HJ *et al*. 2011 Amine-modified single-walled carbon nanotubes protect neurons from injury in a rat stroke model. *Nat. Nanotechnol.* **6**, 121–125. (doi:10.1038/nnano.2010.281)
7. Kam NWS, O'Connell M, Wisdom JA, Dai H. 2005 Carbon nanotubes as multifunctional biological transporters and near-infrared agents for selective cancer cell destruction. *Proc. Natl Acad. Sci. USA* **102**, 11 600–11 605. (doi:10.1073/pnas.0502680102)
8. Sharma P, Brown S, Walter G, Santra S, Moudgil B. 2006 Nanoparticles for bioimaging. *Adv. Colloid Interface* **123–126**, 471–485. (doi:10.1016/j.cis.2006.05.026)
9. Erathodiyil N, Ying JY. 2011 Functionalization of inorganic nanoparticles for bioimaging applications. *Accounts Chem. Res.* **44**, 925–935. (doi:10.1021/ar2000327)
10. Leamon CP, Reddy JA. 2004 Folate-targeted chemotherapy. *Adv. Drug Deliver Rev.* **56**, 1127–1141. (doi:10.1016/j.addr.2004.01.008)
11. Farokhzad OC, Cheng J, Teply BA, Sherifi I, Jon S, Kantoff PW, Richie JP, Langer R. 2006 Targeted nanoparticle-aptamer bioconjugates for cancer chemotherapy *in vivo*. *Proc. Natl Acad. Sci. USA* **103**, 6315–6320. (doi:10.1073/pnas.0601755103)
12. Gehl J, Boesgaard M, Paaske T, Jensen BV, Dombernowsky P. 1996 Combined doxorubicin and paclitaxel in advanced breast cancer: effective and cardiotoxic. *Ann. Oncol.* **7**, 687–693. (doi:10.1093/oxfordjournals.annonc.a010717)
13. Madsen S-K, Mooney DJ. 2000 Delivering DNA with polymer matrices: applications in tissue engineering and gene therapy. *Pharm. Sci. Technol. Today* **3**, 381–384. (doi:10.1016/S1461-5347(00)00305-9)
14. Koyama S, Haniu H, Osaka K, Koyama H, Kuroiwa N, Endo M, Kim YA, Hayashi T. 2006 Medical application of carbon-nanotube-filled nanocomposites: the microcatheter. *Small* **2**, 1406–1411. (doi:10.1002/smll.200500416)
15. Tabet L, Bussy L, Setyan A, Simon-Deckers A, Rossi MJ, Boczkowski J, Lanone S. 2011 Coating carbon nanotubes with a polystyrene based polymer protects against pulmonary toxicity. *Part. Fibre Toxicol.* **8**, 1–13. (doi:10.1186/1743-8977-8-3)
16. Subbiah R, Veerapandian M, Yun K. 2010 Nanoparticles: functionalization and multifunctional applications in biomedical sciences. *Curr. Med. Chem.* **17**, 4559–4577. (doi:10.2174/092986710794183024)
17. Nel A, Xia T, Madler L, Li N. 2006 Toxic potential of materials at the nanolevel. *Science* **311**, 622–627. (doi:10.1126/science.1114397)
18. Manna SK, Sarkar S, Barr J, Wise K, Barrera EV, Jejelowo O, Rice-Ficht AC, Ramesh GT. 2005 Single-walled carbon nanotube induces oxidative stress and activates nuclear transcription factor-κB in human keratinocytes. *Nano Lett.* **5**, 1676–1984. (doi:10.1021/nl0507966)
19. Worle-Knirsch JM, Pulskamp K, Krug HF. 2006 Oops they did it again! Carbon nanotubes hoax scientists in viability assays. *Nano Lett.* **6**, 1261–1268. (doi:10.1021/nl060177c)
20. Davoren M, Herzog E, Casey A, Cottineau B, Chambers G, Byrne HJ, Lyng FM. 2007 *In vitro* toxicity evaluation of single walled carbon nanotubes on human A549 lung cells. *Toxicol. In Vitro* **21**, 438–448. (doi:10.1016/j.tiv.2006.10.007)
21. Subbiah R, Lee H, Veerapandian M, Sadhasivam S, Seo S-W, Yun K. 2011 Structural and biological evaluation of a multifunctional SWCNT-Ag NPs-DNA/PVA bio-nanofilm. *Anal. Bioanal. Chem.* **400**, 547–560. (doi:1007/s00216-011-4757-1)
22. Hitoshi K, Katoh M, Suzuki T, Ando Y, Nadai M. 2011 Differential effects of single-walled carbon nanotubes on cell viability of human lung and pharynx carcinoma cells. *J. Toxicol. Sci.* **36**, 379–387. (doi:10.2131/jts.36.379)
23. Coccini T, Roda E, Sarigiannis DA, Mustarelli P, Quartarone E, Profumo A, Manzoa L. 2010 Effects of water-soluble functionalized multi-walled carbon nanotubes examined by different cytotoxicity methods in human astrocyte D384 and lung A549 cells. *Toxicology* **269**, 41–53. (doi:10.1016/j.tox.2010.01.005)
24. Mu Q, Broughton DL, Yan B. 2009 Endosomal leakage and nuclear translocation of multiwalled carbon nanotubes: developing a model for cell uptake. *Nano Lett.* **9**, 4370–4375. (doi:10.1021/nl902647x)
25. Kagan KE *et al*. 2006 Direct and indirect effects of single walled carbon nanotubes on Raw 264.7 macrophages: role of iron. *Toxicol. Lett.* **165**, 88–100. (doi:10.1016/j.toxlet.2006.02.001)
26. Huczko A, Lange H. 2001 Carbon nanotubes: experimental evidence for a null risk of skin irritation and allergy. *Fullerene Sci. Technol.* **9**, 247–250. (doi:10.1081/FST-100102972)
27. Warheit DB, Laurence BR, Reed KL, Roach DH, Reynolds GAM, Webb TR. 2004 Comparative pulmonary toxicity assessment of single-wall carbon nanotubes in rats. *Toxicol. Sci.* **77**, 117–125. (doi:10.1093/toxsci/kfg228)
28. Pantarotto D, Partidos CD, Hoebeke J, Brown F, Kramer ED, Briand J-P, Muller S, Prato M, Bianco A. 2003 Immunization with peptide-functionalized carbon nanotubes enhances virus-specific neutralizing antibody responses. *Chem. Biol.* **10**, 961–966. (doi:10.1016/j.chembiol.2003.09.011)
29. Cherukuri P, Gannon CJ, Leeuw TK, Schmidt HK, Smalley RE, Curley SA, Weisman RB. 2006 Mammalian pharmacokinetics of carbon nanotubes using intrinsic near-infrared fluorescence. *Proc. Natl Acad. Sci. USA* **103**, 18 882–18 886. (doi:10.1073/pnas.0609265103)
30. Hussain MA, Kabir MA, Sood AK. 2009 On the cytotoxicity of carbon nanotubes. *Curr. Sci.* **96**, 664–673.
31. Kayat J, Gajbhiye V, Tekade RK, Jain NK. 2011 Pulmonary toxicity of carbon nanotubes: a systematic report. *Nanomedicine* **7**, 40–49. (doi:10.1016/j.nano.2010.06.008)
32. Casey A, Davoren M, Herzog E, Lyng FM, Byrne HJ, Chambers G. 2007 Probing the interaction of single walled carbon nanotubes within cell culture medium as a precursor to toxicity testing. *Carbon* **45**, 34–40. (doi:10.1016/j.carbon.2006.08.009)
33. Dong L, Joseph KL, Witkowski CM, Craig MM. 2008 Cytotoxicity of single-walled carbon nanotubes suspended in various surfactants. *Nanotechnology* **19**, 1–5. (doi:10.1088/0957-4484/19/25/255702)
34. Porter AE, Gass M, Bendall JS, Muller K, Goode A, Skepper JN, Midgley PA, Welland M. 2009 Uptake of noncytotoxic acid-treated single-walled carbon nanotubes into the cytoplasm of human macrophage cells. *ACS Nano* **3**, 1485–1492. (doi:10.1021/nn900416z)
35. Ren J, Shen S, Wang D, Xi Z, Guo L, Pang Z, Qian Y, Sun X, Jiang X. 2012 The targeted delivery of anticancer drugs to brain glioma by pegylated oxidized multi-walled carbon nanotubes modified with angiopep-2. *Biomaterials* **33**, 3324–3333. (doi:10.1016/j.biomaterials.2012.01.025)
36. Caro C, Castillo PM, Klippstein R, Pozo D, Zaderenko AP. 2010 Silver nanoparticles: sensing and imaging applications. In *Silver nanoparticles* (ed. D Pozo Perez). New York, NY: In-Tech.
37. Nuttelman CR, Henry SM, Anseth KS. 2002 Synthesis and characterization of photocrosslinkable, degradable poly(vinyl alcohol)-based tissue engineering scaffolds. *Biomaterials* **23**, 3617–3626. (doi:10.1016/S0142-9612(02)00093-5)
38. Chaouat M, Visage CL, Baille WE, Escoubet B, Chaubet F, Mateescu MA, Letourneur D. 2008 A novel cross-linked poly(vinyl alcohol) (PVA) for vascular grafts. *Adv. Funct. Mater.* **18**, 2855–2861. (doi:10.1002/adfm.200701261)
39. Pal K, Banthia AK, Majumdar DK. 2009 Polymeric hydrogels: characterization and biomedical applications. *Des. Monomers Polym.* **12**, 197–220. (doi:10.1163/156855509X436030)
40. Valente AJM, Cruz SMA, Morán MC, Murtinho DB, Muniz EC, Miguel MG. 2010 Release of DNA from cryogel PVA-DNA membranes. *Express Polym. Lett.* **4**, 480–487. (doi:10.3144/expresspolymlett.2010.61)
41. Quintavalle M, Elia L, Price JH, Heynen-Genel S, Sara A, Courtneidge SA. 2011 A cell-based high-content screening assay reveals activators and inhibitors of cancer cell invasion. *Sci. Signal.* **4**, 1–9. (doi:10.1126/scisignal.2002032)
42. Tomankova K, Kolarova H, Vujtek M, Zapletalova H. 2007 Study of cancer cells used atomic force

microscopy. In *Modern research and educational topics in microscopy* (eds A Mendez-Vilas, J Diaz), pp. 23–28. Badajoz, Spain: Formatex Research Center.

43. Howland R, Benatar L. 1998 *A practical guide to scanning probe microscopy* (ed. Christy Symanski), 1st edn. Darby, PA: Diane Publishing Company.
44. Bizzarri AR, Cannistraro S. 2010 The application of atomic force spectroscopy to the study of biological complexes undergoing a biorecognition process. *Chem. Soc. Rev.* **39**, 734–749. (doi:10.1039/B811426A)
45. Müller DJ, Dufrêne YF. 2008 Atomic force microscopy as a multifunctional molecular toolbox in nanobiotechnology. *Nat. Nanotechnol.* **3**, 261–269. (doi:10.1038/nnano.2008.100)
46. Evans EA, Calderwood DA. 2007 Forces and bond dynamics in cell adhesion. *Science* **316**, 1148–1153. (doi:10.1126/science.1137592)
47. You HX, Yu L. 1999 Atomic force microscopy imaging of living cells: progress, problems and prospects. *Method Cell. Sci.* **21**, 1–17. (doi:10.1023/A:1009876320336)
48. Wilusz RE, DeFrate LE, Guilak F. 2012 Immunofluorescence-guided atomic force microscopy to measure the micromechanical properties of the pericellular matrix of porcine articular cartilage. *J. R. Soc. Interface* **9**, 2997–3007. (doi:10.1098/rsif.2012.03141742-5662)